A Fast Semi-Analytic Approach for Combined Electromigration and Thermomigration Analysis for General Multisegment Interconnects

Liang Chen, *Student Member, IEEE*, Sheldon X.-D. Tan, *Senior Member, IEEE*, Zeyu Sun, *Student Member, IEEE*, Shaoyi Peng, *Student Member, IEEE*, Min Tang, *Member, IEEE*, and Junfa Mao, *Fellow, IEEE*

***Abstract*—Considering temperature gradient or thermomigration (TM) impacts on electromigration (EM) due to Joule heating was less studied in the past. In this article, we propose a new semi-analytical stress transient analysis method to consider both EM and TM effects for general multisegment interconnects. The new method is based on the separation of variables (SOVs) approach to find the analytic solution of coupled EM-TM partial differential equation (PDE). The algorithm consists of several steps. We first develop analytic solutions to compute the steady-state temperature distribution of multisegment wires. Based on this, we derive closed-form solutions for steady-state hydrostatic stress distribution in the context of thermal gradients due to Joule heating for multisegment interconnect wires. With the steady-state stress distribution, the coupled EM-TM PDE can be homogenized and solved by the SOV method. To deal with temperature/position-dependent diffusivity of metal migration process due to nonuniform temperature distribution, we utilize a piecewise linear technique to approximate the position-dependent diffusivity. The numerical results on multisegment interconnects show that the proposed method has negligible error loss compared to commercial finite element analysis software COMSOL but is about an order of magnitude faster than COMSOL with 10× less memory footprint. The numerical results further show that temperature gradient due to Joule heating indeed has significant impacts on the EM failure process.**

***Index Terms*—Analytical thermal model, electromigration (EM), Joule heating, separation of variables (SOVs) method, temperature gradient effects.**

Manuscript received December 18, 2019; revised March 23, 2020; accepted May 3, 2020. Date of publication May 12, 2020; date of current version January 20, 2021. This work was supported in part by NSF under Grant CCF-1527324, Grant CCF-1816361, and Grant OISE-1854276. The work of Liang Chen was supported by the China Scholarship Council under Grant 201806230078. This article was recommended by Associate Editor N. Wong. *(Corresponding author: Sheldon X.-D. Tan.)*

Liang Chen was with the University of California at Riverside, Riverside, CA 92521 USA. He is now with the Key Laboratory of Ministry of Education of China for Research of Design and Electromagnetic Compatibility of High Speed Electronic Systems, Shanghai Jiao Tong University, Shanghai 200240, China, and also with the Department of Electrical and Computer Engineering, University of California at Riverside, Riverside, CA 92521 USA (e-mail: chenliang_sjtu@sjtu.edu.cn).

Sheldon X.-D. Tan, Zeyu Sun, and Shaoyi Peng are with the Department of Electrical and Computer Engineering, University of California at Riverside, Riverside, CA 92521 USA (e-mail: stan@ece.ucr.edu).

Min Tang and Junfa Mao is with the Key Laboratory of Ministry of Education of China for Research of Design and Electromagnetic Compatibility of High Speed Electronic Systems, Shanghai Jiao Tong University, Shanghai 200240, China.

Digital Object Identifier 10.1109/TCAD.2020.2994271

I. Introduction

DUE TO the increasing current densities and decreasing dimensions of the interconnects, electromigration (EM) induced aging and failure effects remain the top reliability concerns for modern VLSI chips in 7-nm technology and below. Therefore, it is important to develop more accurate and less conservative EM sign-off and validation [1]. However, it is well accepted that existing Black and Blech-based EM models are subject to growing criticism due to over conservativeness and they only work for a single wire segment [2], [3].

To mitigate the existing problem in EM models, a number of physics-based EM models and assessment techniques have been proposed [1], [4]–[16]. Those EM models primarily focus on solving the partial differential equation (PDE) (called Korhonen's equation) of hydrostatic stress evolution in the confined multisegment wires subject to blocking material boundary conditions.

However, most of those EM models do not consider the temperature gradient impacts on the metal migration process. Instead, most of those approaches just assume constant wire temperature. However, recent study [16] shows that the temperature gradient effects can be quite significant (almost in the same magnitude as the current induced migration) due to the Joule heating effects. This situation will become even worse as technology advances to smaller features and 3-D stacked integration, in which higher power density, larger Joule heating, and larger thermal resistances due to stacking will lead to even higher temperature and temperature gradients across chip [17]. To better illustrate the importance of thermomigration (TM) effect, we show the ratio of TM flux over EM flux defined below under different conditions

$$\left|\frac{J_{\mathrm{TM}}}{J_{\mathrm{EM}}}\right| = \frac{Q/T \cdot |\frac{\partial T}{\partial x}|}{eZ\rho j} \quad (1)$$

where Q is the specific heat of transport, T is the temperature, e is the elementary charge, Z is the effective charge number, ρ is the electrical resistivity, j is the current density, and J_{TM} and J_{EM} are TM flux and EM flux, respectively. Fig. 1 shows the TM over EM ratio in (1) with different Q values and temperature gradients, where Q is ranged from 0.09 eV to 0.9 eV for different techniques [18]. As both Q values and temperature gradients (larger current densities) increase, the TM effect

0278-0070 © 2020 IEEE. Personal use is permitted, but republication/redistribution requires IEEE permission.
See https://www.ieee.org/publications/rights/index.html for more information.

Authorized licensed use limited to: Univ of Calif Riverside. Downloaded on June 24,2026 at 00:44:23 UTC from IEEE Xplore. Restrictions apply.

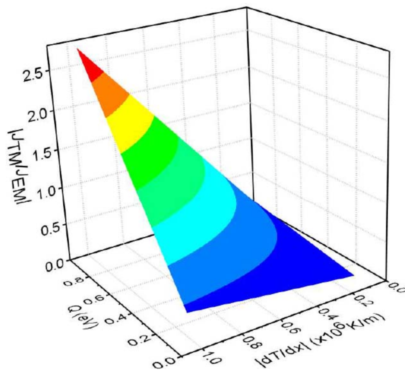

Fig. 1. Effect of the heat of transport Q and temperature gradient $|dT/dx|$ on the ratio of TM flux to EM flux.

becomes more significant and can be even larger than the EM effect.

In this article, we propose a new semi-analytical solution to compute the transient hydrostatic stress evolution considering both EM and TM for the general multisegment interconnect trees. Our new contributions are as followings.

1) First, an accurate analytical thermal model is employed to capture the nonuniform temperature distribution of the interconnects due to Joule heating for a single wire. On top of this, we develop a closed-form expression for temperature distribution of multisegment wires. With this result, we derive a more general and accurate analytical formula for steady-state stress distribution based on the computed nonuniform temperature distribution.
2) Second, with the steady-state stress distribution, the coupled EM-TM PDE can be easily homogenized and solved by the separation of variables (SOVs) method, in which Bessel function was derived as the eigenfunctions in the new SOV method, which is different from that in [19] and [20]. To deal with temperature/position-dependent diffusivity of the metal migration process due to nonuniform temperature distribution, we use a piecewise linear technique to approximate the position-dependent diffusivity, which is more suitable for the nonuniform diffusivity in contrast to stepwise uniform approximation [21].
3) Third, compared with constant temperature, the effects of nonuniform temperature distribution on EM void nucleation phase for large multisegment interconnect trees are studied, which shows that temperature gradient due to Joule heating indeed has significant impacts on the EM failure process. The numerical results on multisegment interconnects show that the proposed method has negligible error loss compared to commercial finite element software COMSOL but is about an order of magnitude faster than COMSOL with $10\times$ less memory footprint.

The remainder of this article is organized as follows. Section II reviews the physics-based EM model considering TM effects. Section III gives a coupled EM-TM PDE describing hydrostatic stress. Section IV presents the analytical thermal model describing the temperature distribution of the interconnects and develops an approach to extract effective thermal length. Section V presents an accurate and analytical solution for steady-state EM-TM stress assessment. Section VI proposes a novel and efficient semi-analytical EM-TM method to estimate the hydrostatic stress evolution under nonuniform temperature distribution. Section VII shows numerical results for the proposed method and comparison against the commercial software COMSOL. Section VIII concludes this article.

II. Review of Relevant Work

Metal atoms migrate in the presence of thermal gradients. This effect is called *Soret Effect* or TM [22]. The TM effects have been studied in the past and should be seriously considered in current and future interconnects of ICs [23]–[26]. It has been experimentally observed that temperature gradient $|dT/dx|$ can easily exceed 0.1 K/μm [16], [23], [24], [26], [27]. Li *et al.* [28] showed that temperature changes rapidly in the short and advanced interconnects using both measurement method and finite element-based ANSYS simulation. Temperature contour map obtained by scanning Joule expansion microscopy shows that Joule heating with current density 3.13×10^{10}A/m^2 leads to temperature rise 30 K on an interconnect of length 9 μm [29]. The large temperature gradients can cause significant TM, which can be in the same magnitude as EM [16], [24], [26]. Also, experimental data shows that thermal gradient has significant impacts on the EM-induced time to failure (TTF) for power electronics [25]. This article shows that thermal gradient of 0.19 K/μm can lead to 50% TTF reduction even with low oven temperature. In [24], the experiments and simulation show that when the direction of temperature gradient (25 K/200 μm) changes from positive to negative, the mean TTF (MTTF) improves by 213%. When the directions of temperature gradient and current are same, temperature gradient reduces MTTF by 57%. If they are in the opposite directions, temperature gradient improves MTTF by 33%. The effect of TM and EM on microelectronics solder joints is also studied with experiments and simulation in [30]. This article shows that with 2.4×10^{10}A/m^2 current density, 376 K hot temperature and 366 K cold temperature in the experiments, the test vehicle fails after 693 h. It can be seen that crack in the solder joints which are stressed by TM+EM forces is the worst among the TM, TM-EM, and TM+EM cases. As a result, TM effect has to be seriously considered due to significant Joule heating in modern ICs.

However, many existing EM methods only consider the transient/temporal thermal effects when solving the Korhonen's equation or derive analytic models to estimate transient EM stress under time-varying temperature [8], [10], [11], [31], [32]. Those works do not consider the spatial temperature or thermal gradient impacts on the multisegments. After that, some research efforts are carried out recently to investigate EM considering the TM effects [16], [18], [33]–[36]. A coupled EM-TM equation based on Korhonen's equation is proposed and well-accepted to estimate hydrostatic stress evolution due to EM, TM, and stressmigration (SM).

Authorized licensed use limited to: Univ of Calif Riverside. Downloaded on June 24,2026 at 00:44:23 UTC from IEEE Xplore. Restrictions apply.

To efficiently and accurately solve the Korhonen's equation, a number of numerical and analytic solutions are proposed recently, such as finite difference-based methods [12], [37], [38], finite element-based methods for post-voiding phase analysis [15], [39], and efficient analytical or semi-analytic solutions [6], [16], [19], [20], [40], [41]. Among them, SOV method [19], [20] is a promising semi-analytic method for general multisegment interconnect trees.

However, applying SOV method for the coupled EM-TM equation becomes challenging as one has the location/temperature dependence of diffusivity of metal migration due to the presence of spatial thermal gradients. Recently Abbasinasab *et al.* [16], [18], [36] proposed analytical solutions for both transient and steady states of the EM-TM model. However, their steady-state solution has more restricted assumption in which the temperature of surrounding dielectrics needs to be the average temperature of two end nodes in a segment. Furthermore, the analytical transient method only works for constant diffusivity of EM. For multibranch interconnects structure, this method has to recompute the coefficients to satisfy the boundary conditions for all junctions in each time point, which requires very expensive computational cost. Therefore, more efficient and accurate transient coupled EM-TM analysis techniques considering spatial temperature-dependent diffusivity are highly desirable.

III. Electromigration Model Considering Thermal Gradient Effects

EM is a diffusion phenomenon of the migration of metal atoms due to several driving forces. The momentum exchange from conducting electrons to metal atoms creates metal atoms tension at the cathode end and a corresponding metal compression at the anode ends of the metal wire. The temperature gradient is another important driving force to move atoms from hot to cool places. The lasting migration process increases the hydrostatic stress, which is a prime cause of forming void at cathode and hillock at anode of the interconnects. As the stress reaches the critical value, voids can be created. To make matters worse, the void causes open circuit and the hillock leads to short circuit in the interconnects, which is called EM-induced failure and a major reliability problem in 3-D ICs.

The total atomic flux is the sum of the three fluxes due to EM, SM, and TM, expressed as [16], [18], [33]–[36]

$$\begin{aligned} J &= J_{\text{EM}} + J_{\text{SM}} + J_{\text{TM}} \\ &= -D_v\left(\frac{\Omega}{k_BT}C_v\frac{\partial\sigma}{\partial x} - C_v\frac{eZ\rho j}{k_BT} - \frac{Q}{k_BT^2}C_v\frac{\partial T}{\partial x}\right) \end{aligned} \tag{2}$$

where D_v is the vacancy diffusivity, C_v is the vacancy concentration, k_B is Boltzmann's constant, Ω is the atomic volume, and σ is the hydrostatic stress.

Then, Korhonen's equations considering temperature gradients can be rewritten as [33]

$$\frac{\partial\sigma}{\partial t} = \frac{\partial}{\partial x}\left[\kappa(x)\left(\frac{\partial\sigma}{\partial x} - \frac{eZ\rho j}{\Omega} - \frac{Q}{\Omega T}\frac{\partial T}{\partial x}\right)\right] \tag{3}$$

where $\kappa(x) = D_a(T(x))B\Omega/(k_BT(x))$ is a position-dependent diffusivity due to nonuniform temperature, and $D_a = D_0\exp(-E_a/(k_BT))$ is atomic diffusion coefficient. D_0 is a constant and E_a is the EM activation energy. Equation (3) can be viewed as coupled EM and TM equation for hydrostatic stress and its detail derivation is described in Appendix A.

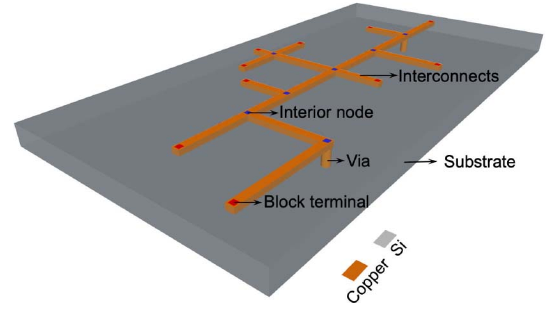

Fig. 2. 3-D view of a general multisegment interconnects.

Real on-chip power grid networks consist of many single branches, which are connected with each other by the junction, as shown in Fig. 2. Several researches show the hydrostatic stress cannot be computed in the individual branch because each branch is not independent [1], [6], [19], [41]. To consider these connected effects, for a general interconnect wires with n nodes, including p interior junction nodes $x_r \in \{x_{r1}, x_{r2}, \ldots, x_{rp}\}$ and q block terminals $x_b \in \{x_{b1}, x_{b2}, \ldots, x_{bq}\}$, as shown in Fig. 2 (blue nodes for x_r and red nodes for x_b), the hydro-static stress distribution $\sigma(x, t)$ along the wire is described by the following coupled EM-TM equation:

$$\begin{aligned} &\frac{\partial\sigma_{ij}}{\partial t} = \frac{\partial}{\partial x}\left[\kappa_{ij}(x)\left(\frac{\partial\sigma_{ij}}{\partial x} - S_{ij} - M_{ij}\right)\right],\ \ t > 0 \\ &\text{BC}: \sigma_{ij_1}(x_i, t) = \sigma_{ij_2}(x_i, t),\ \ t > 0 \\ &\text{BC}: \sum_{ij}\kappa_{ij}(x_r)\left(\left.\frac{\partial\sigma_{ij}}{\partial x}\right|_{x=x_r} - S_{ij} - M_{ij}\right)\cdot n_r = 0,\ \ t > 0 \\ &\text{BC}: \kappa_{ij}(x_b)\left(\left.\frac{\partial\sigma_{ij}}{\partial x}\right|_{x=x_b} - S_{ij} - M_{ij}\right) = 0,\ \ t > 0 \\ &\text{IC}: \sigma_{ij}(x, 0) = \sigma_{ij,T} \end{aligned} \tag{4}$$

where ij denotes a branch connected to nodes i and j, n_r represents the unit inward normal direction of the interior junction node r on branch ij, which is $+1$ for right direction and -1 for left direction of branch with assumption of $x_i < x_j$. $S_{ij} = eZ\rho j/\Omega$ is EM flux and $M_{ij} = Q/(\Omega T)\cdot\partial T/\partial x$ for TM flux for branch ij. $\sigma_{ij,T}$ is the initial thermal-induced residual stress for segment or branch ij. Fig. 3(left) shows a cross interconnect tree, which is a two dimensions structure. To calculate the hydrostatic stress efficiently and conveniently in this article, we reduced 2-D problem (x-y) to 1-D problem (x) which is described by (4). By performing such 2-D to 1-D mapping, we will end up with the same value of x but at different wire segments, as shown in Fig. 3(right). The value of x only represents the relative position in each segment.

Based on the physical EM-TM model, we can carry out a combined EM and TM analysis for general multisegment interconnects, as shown in Fig. 4. At the beginning, the dissipated power calculated by Joule heating due to high current density is treated as heat source in thermal analysis.

Authorized licensed use limited to: Univ of Calif Riverside. Downloaded on June 24,2026 at 00:44:23 UTC from IEEE Xplore. Restrictions apply.

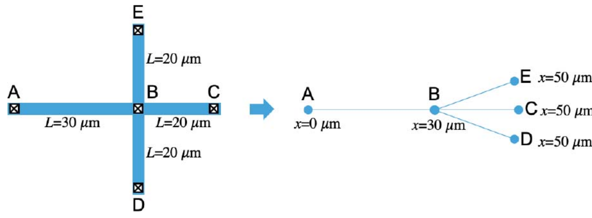

Fig. 3. 2-D problem to 1-D problem mapping in the proposed analytic solution.

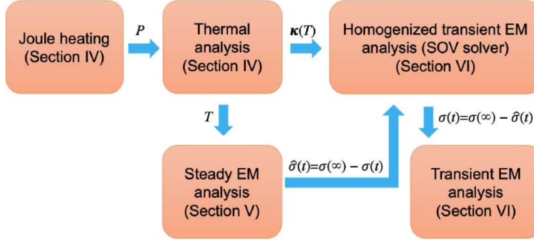

Fig. 4. Algorithmic flow of the proposed combined EM and TM analysis.

Then, we develop an analytical temperature solution of the interconnects, as described in Section IV. With temperature distribution, steady-state solution of coupled EM-TM equation can be obtained, as shown in Section V. After that, considering nonuniform diffusivity $\kappa(T)$, we use steady-state solution to homogenize the EM-TM (4). To solve homogeneous EM-TM equation, an efficient SOVs method is proposed to do transient analysis. Finally, we can obtain the original transient response of hydrostatic stress by inverse transformation, as shown in Section VI.

IV. Thermal Analysis of Interconnects Due to Joule Heating

To consider the nonuniform temperature effects, we have to capture the temperature profiles of the interconnects due to Joule heating. Generally, heat conduction equation with boundary conditions is utilized to model heat transfer and obtain temperature [42]. Many numerical methods, such as finite element method and finite difference method, have been proposed to solve the heat conduction equation. Numerical methods require expensive computation cost for very large scale integrated (VLSI) circuits. Because of uniform structure along the interconnects, we can reduce 3-D structure to 1-D problem and develop an analytical solution for heat conduction on the interconnects [16], [43]. However, this method only works for a single wire, not for general multisegment interconnects. In addition, the expression for effective thermal length Γ is not accurate enough. Based on that, we develop a novel analytical approach to characterize thermal behavior of general multisegment interconnects, which is efficient and accurate.

Specifically, the dissipated power density due to Joule heating is calculated by

$$P = \frac{I^2 R}{V} = \frac{(jA)^2 \rho \frac{L}{A}}{LA} = j^2 \rho \tag{5}$$

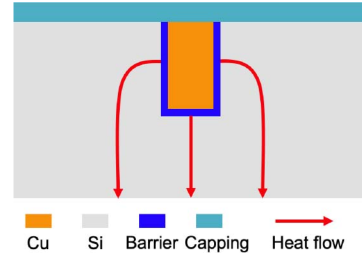

Fig. 5. Cross view of a interconnect.

where I is the current, R is the resistance, V is the volume, A is the cross sectional area, and L is the length of the interconnects.

For interconnect wires, we can consider this problem as 1-D problem. Then the governing heat equation along the Cu interconnects can be described by

$$\kappa_{\mathrm{Cu}} \frac{\partial^2 T(x)}{\partial x^2} - h_{\mathrm{eff}}(T - T_0) + j^2 \rho = 0 \tag{6}$$

where κ_{Cu} is thermal conductivity of Cu interconnects, and h_{eff} is the coefficient of convective heat transfer from Cu interconnect to surrounding substrate, T_0 is temperature on the bottom side of Si substrate. The item $h_{\mathrm{eff}}(T - T_0)$ in (6) is introduced to represent heat which flows from interconnects to surrounding dielectric, as shown in Fig. 5. With this item, we can reduce complex 3-D thermal analysis of the interconnects to 1-D problem.

With the boundary conditions $T(-[L/2]) = T_1$ and $T(L/2) = T_2$, the solution of (6) is obtained by [18], [43]

$$T(x) = \left[\overline{T} - (T_0 + T_m)\right]\mathrm{sech}\left(\frac{L}{2\Gamma}\right)\cosh\left(\frac{x}{\Gamma}\right) + T_n \mathrm{csch}\left(\frac{L}{2\Gamma}\right)\sinh\left(\frac{x}{\Gamma}\right) + (T_0 + T_m) \tag{7}$$

where

$$\overline{T} = \frac{T_1 + T_2}{2}, T_n = \frac{T_2 - T_1}{2}, T_m = \frac{j^2 \rho \Gamma^2}{\kappa_{\mathrm{Cu}}} \tag{8}$$

where Γ can be viewed as effective thermal length, which can be expressed as [43]

$$\Gamma = \sqrt{\frac{\kappa_{\mathrm{Cu}}}{h_{\mathrm{eff}}}} \approx \sqrt{\frac{\kappa_{\mathrm{Cu}} t_{\mathrm{Cu}} t_{\mathrm{ILD}}}{\kappa_{\mathrm{ILD}}}} \tag{9}$$

where κ_{ILD} is the thermal conductivity of dielectric, t_{ILD} and t_{Cu} are the thickness of dielectric and copper, respectively. Approximated (9) illustrates Γ is determined by the dimensions and thermal conductivity of interconnect and surrounding dielectrics, as shown in Fig. 5. However, expression (9) only gives an approximated value, which may lead to inaccurate temperature results. To get accurate estimation of Γ, we propose to use finite element-based COMSOL to extract the effective thermal length of the solution (7). Note for a given technology node, in general we can assume Γ is the same as first order approixmation across the whole chip as the cross section of interconnects in a chip does not change signfiicantly. If necessary, we can compute the Γ for each specific layer as well.

Authorized licensed use limited to: Univ of Calif Riverside. Downloaded on June 24,2026 at 00:44:23 UTC from IEEE Xplore. Restrictions apply.

First, finite element analysis based on COMSOL is performed to calculate temperature $T_i \in \mathbf{T}(i = 1, \ldots, N)$ at corresponding position $x_i \in \mathbf{x}(i = 1, \ldots, N)$ along the Cu interconnects. $\mathbf{T}$ and $\mathbf{x}$ are vectors, which represent temperature and position, respectively.

Second, we can tune the value of Γ and fit the reference results $\mathbf{T}$ and $\mathbf{x}$ by using expression (7). To estimate Γ accurately, the destination is to minimize error ϵ defined as follows:

$$\epsilon = \frac{1}{N}\sum_{i=1}^{N}(T_i - T(x_i, \Gamma))^2 = \frac{[\mathbf{T} - T(\mathbf{x}, \Gamma)]^T[\mathbf{T} - T(\mathbf{x}, \Gamma)]}{N}. \quad (10)$$

Instead of tuning the value of Γ manually, the accurate Γ is searched automatically by the Newton's iteration

$$\Gamma_{n+1} = \Gamma_n + \frac{[\mathbf{T} - T(\mathbf{x}, \Gamma_n)]^T[\mathbf{T} - T(\mathbf{x}, \Gamma_n)]}{2[\mathbf{T} - T(\mathbf{x}, \Gamma_n)]^T \frac{\partial T(\mathbf{x}, \Gamma)}{\partial \Gamma}|_{\Gamma=\Gamma_n}} \quad (11)$$

with the initial value from (9). Notice Γ can also be obtained by directly measurement or by computing the accurate coefficient of the effective convective heat transfer, h_{eff}, as shown in (9).

For general multisegment wires, we assume that each wire segment ij has a direction defined for the sign of its heat flux $\mathbf{q}_{ij}(x)$ at interior junction nodes $x_r \in \{x_{r1}, x_{r2}, \ldots, x_{rp}\}$. Then we observe that heat flux conservation is satisfied at location x_r, which is described by

$$\sum_{ij} \mathbf{q}_{ij}(x_r) = 0. \quad (12)$$

We note that this heat flux conservation ignores the heat loss to the surrounding dielectrics at x_r, which we assume is very small in general.

At the block terminals $x_b \in \{x_{b1}, x_{b2}, \ldots, x_{bq}\}$, heat flux flows from the terminal to its surrounding dielectrics due to convective boundary condition, which is modeled by

$$-\mathbf{q}_{ij}(x_b) \cdot \mathbf{n}_b = h_b\big(T_{ij}(x_b) - T_0\big) \quad (13)$$

where h_b is the convective coefficient. The heat flux and temperature are related by Fourier's law, which is expressed as

$$\mathbf{q} = -\kappa_{\text{Cu}}\nabla T. \quad (14)$$

Therefore, substituting (14) to boundary conditions (12) and (13), we have

$$\text{BC} : \sum_{ij} \frac{\partial T_{ij}(x)}{\partial x}\bigg|_{x=x_r} \cdot n_r = 0$$
$$\text{BC} : \frac{\partial T_{ij}(x)}{\partial x}\bigg|_{x=x_b} \cdot n_b = \Gamma_b^{-2}\big(T_{ij}(x_b) - T_0\big) \quad (15)$$

where terminal thermal length is given by

$$\Gamma_b = \sqrt{\frac{\kappa_{\text{Cu}}}{h_b}}. \quad (16)$$

Finally, based on boundary conditions (15), temperature expression (7) and its derivative, we can form the linear equations

$$\mathbf{A} \cdot \boldsymbol{\beta} = \mathbf{B} \quad (17)$$

where $\mathbf{A}$ is a $(p+q) \times (p+q)$ matrix, $\mathbf{B}$ is a $(p+q) \times 1$ vector and the vector to be determined is represented by

$$\boldsymbol{\beta} = \big[T_{ij}(x_1), T_{ij}(x_2), \ldots, T_{ij}(x_n)\big]^T. \quad (18)$$

The elements of matrix $\mathbf{A}$ are connected with a tree structure, which can be solved linearly and efficiently. Once the temperature of n nodes is obtained, temperature distribution along the interconnects can be determined by (7).

We notice that at terminal nodes (vias typically), the related elements of $\boldsymbol{\beta}$ are known already, which are called $\boldsymbol{\beta}_d$. To solve this problem, we reorder and decompose (17), which is expressed as

$$\begin{bmatrix} \mathbf{A}_{11} & \mathbf{A}_{12} \\ \mathbf{A}_{21} & \mathbf{A}_{22} \end{bmatrix} \cdot \begin{bmatrix} \boldsymbol{\beta}_u \\ \boldsymbol{\beta}_d \end{bmatrix} = \begin{bmatrix} \mathbf{B}_1 \\ \mathbf{B}_2 \end{bmatrix} \quad (19)$$

where $\boldsymbol{\beta}_u$ denotes unknown elements of $\boldsymbol{\beta}$ and $\boldsymbol{\beta}_d$ represents Dirichlet boundary elements of $\boldsymbol{\beta}$. Therefore, the unknown temperature can be calculated by

$$\boldsymbol{\beta}_u = \mathbf{A}_{11}^{-1}\big(\mathbf{B}_1 - \mathbf{A}_{12} \cdot \boldsymbol{\beta}_d\big). \quad (20)$$

We remark that we only need to consider the steady-state temperature distributions in the multisegment wires in our problem. The reason is that transient behavior of the temperature is not important as temperature changing rates (time constant) is in the range of mili-second for VLSI systems [42], while the time constant of EM is in the range of days or months.

We note that we also need to consider the temperature changing from active devices, which basically are computed by the traditional full-chip thermal analysis or coupled electrical-thermal analysis with proper power modeling for the devices at different levels [42] and many works have been proposed in the past [44]. We can treat the full-chip thermal analysis results as the ambient temperature inputs to the proposed EM analysis, as shown in (6). If the full-chip thermal analysis already includes the Joule-heating analysis, then we can directly use the computed temperature profile for both steady-state hydrostatic stress analysis and transient stress analysis with location dependent EM diffusivity, which will be discussed in following sections.

V. Steady-State Analytic Solution Considering Both Thermomigration and Residual Thermo-Mechanical Stress

In this section, we derive the steady-state solution of the coupled EM-TM equation in (4) considering the nonzero residual initial stress mainly from thermo-mechanical effects. Also, the steady analysis of the EM-TM model will be used to transfer the coupled EM-TM equation into homogeneous one in transient analysis as we show later.

Specifically, let σ_0 is the nonzero initial residual stress of the wire, which may come from thermo-mechanical effects

Authorized licensed use limited to: Univ of Calif Riverside. Downloaded on June 24,2026 at 00:44:23 UTC from IEEE Xplore. Restrictions apply.

during the back end of line (BEOL) process. When the stress distribution comes to steady state, the atom flux no longer changes with time, and the constant atom flux in the wire becomes zero, which leads to

$$J_a = \kappa(x)\left(\frac{\partial \sigma(x,\infty)}{\partial x} - \frac{eZ\rho j}{\Omega} - \frac{Q}{\Omega T}\frac{\partial T}{\partial x}\right) = 0. \quad (21)$$

By integration of (21), we obtain the steady-state stress solution as

$$\sigma(x,\infty) = \frac{eZ\rho j}{\Omega}x + \frac{Q}{\Omega}\ln(T(x)) + C \quad (22)$$

where C is the constant to be determined.

We notice that instead of finding $\sigma(x,\infty)$ for all possible x, we just need to find the $\sigma(x,\infty)$ at the junction nodes $x_r \in \{x_{r1}, x_{r2}, \ldots, x_{rp}\}$ and block terminals $x_b \in \{x_{b1}, x_{b2}, \ldots, x_{bq}\}$. The total number of nodes is $p+q$ with $p+q-1$ wire segments. Then, we need $p+q$ equations to solve for the $p+q$ unknowns.

The difference of the hydrostatic stress at two ends of a wire segment can be written as

$$\sigma(x_i) - \sigma(x_j) = \frac{eZ\rho j}{\Omega}L_{ij} + \frac{Q}{\Omega}\left[\ln(T(x_i)) - \ln(T(x_j))\right]. \quad (23)$$

As a result, we have $p+q-1$ equations already. Now we still need one more equation. By integration of (22), we have

$$\begin{aligned}\int_{x_i}^{x_j} \sigma(x)dx &= \frac{\sigma(x_i)+\sigma(x_j)}{2}L_{ij} \\ &+ \frac{Q}{\Omega}\left[\ln\left(\frac{T_0+T_m}{\sqrt{T_iT_j}}\right)L_{ij} \right.\\ &\left. + \frac{(T_i+T_j-2(T_0+T_m))\Gamma}{(T_0+T_m)}\tanh\left(\frac{L_{ij}}{2\Gamma}\right)\right]. \quad (24)\end{aligned}$$

For general multisegment interconnect trees, with the atom conservation $\int \sigma(x)dx = \int \sigma_0(x)dx$, we obtain the last equation

$$\begin{aligned}\sum_{ij}\left[\frac{\sigma_i+\sigma_j}{2}L_{ij} + \frac{Q}{\Omega}\left(\ln\left(\frac{T_0+T_{m,ij}}{\sqrt{T_iT_j}}\right)L_{ij} \right.\right.\\ \left.\left. + \frac{(T_i+T_j-2(T_0+T_{m,ij}))\Gamma}{(T_0+T_{m,ij})}\tanh\left(\frac{L_{ij}}{2\Gamma}\right)\right)\right] \\ = \int \sigma_0(x)dx. \quad (25)\end{aligned}$$

With the $p+q$ equations, we can obtain the steady-state stress $\sigma(x,\infty)$ at all the nodes that we are interested in.

VI. Transient Stress Solution

In this section, we develop a semi-analytic transient solution for the coupled EM-TM (4) using the SOV method. The SOV method has been applied to solve the Korhonen's equations without considering the thermal effects [19], [20]. However, it is difficult to use the SOV method to solve the EM-TM PDE due to the position-dependent diffusivity of copper wires.

As we can see from Fig. 6, piecewise linear and stepwise constant approximations are used to approximate the nonuniform diffusivity. It is evident that piecewise linear approximation shown in Fig. 6(a) requires less segments while maintaining high accuracy in contrast to stepwise constant approximation [45] shown in Fig. 6(b). Therefore, it is essential to develop piecewise linear approximation-based SOV method to solve the transient EM-TM PDE.

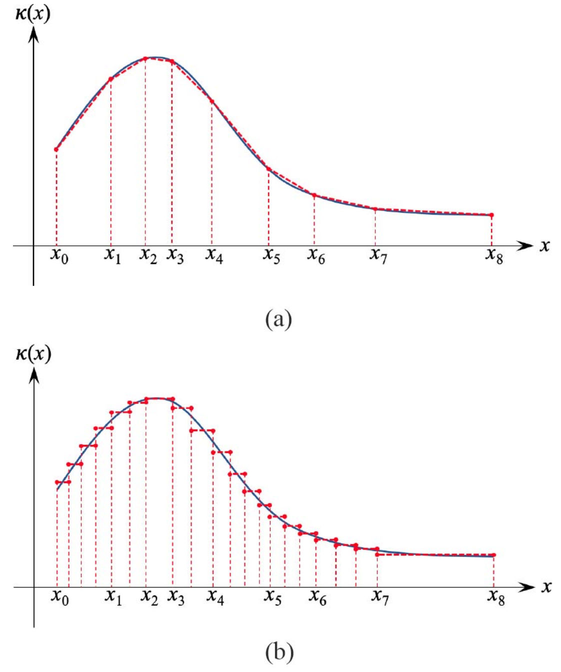

Fig. 6. (a) Piecewise linear approximation. (b) Step-wise constant approximation of diffusion coefficient $\kappa(x)$.

In this article, we employ a piecewise linear approximation to model temperature gradients across a wire. Specifically, as shown in Fig. 6(a), the diffusivity can be approximated by

$$\kappa(x) = \begin{cases} k_1x+b_1 & x_0 \le x < x_1 \\ k_2x+b_2 & x_1 \le x < x_2 \\ \cdots \\ k_nx+b_n & x_{n-1} \le x < x_n. \end{cases} \quad (26)$$

Then, we can homogenize both the governing equation and boundary conditions with following transformation:

$$\hat{\sigma}(x,t) = \sigma(x,\infty) - \sigma(x,t). \quad (27)$$

After that, the EM-TM PDE (4) can be transformed into homogeneous initial-boundary value problem (IBVP), which is described by

$$\frac{\partial \hat{\sigma}_{ij}}{\partial t} = \frac{\partial}{\partial x}\left[\kappa_{ij}(x)\frac{\partial \hat{\sigma}_{ij}}{\partial x}\right], t > 0 \quad (28a)$$

$$\text{BC}: \hat{\sigma}_{ij_1}(x_i,t) = \hat{\sigma}_{ij_2}(x_i,t),\ t>0 \quad (28b)$$

$$\text{BC}: \sum_{ij}\kappa_{ij}(x_r)\frac{\partial \hat{\sigma}_{ij}}{\partial x}\bigg|_{x=x_r}\cdot n_r = 0,\ t>0 \quad (28c)$$

$$\text{BC}: \kappa_{ij}(x_b)\frac{\partial \hat{\sigma}_{ij}}{\partial x}\bigg|_{x=x_b} = 0,\ t>0 \quad (28d)$$

$$\text{IC}: \hat{\sigma}_{ij}(x,0) = \sigma(x,\infty) - \sigma_{ij,T}. \quad (28e)$$

Authorized licensed use limited to: Univ of Calif Riverside. Downloaded on June 24,2026 at 00:44:23 UTC from IEEE Xplore. Restrictions apply.

Applying SOVs method $\hat{\sigma}_{ij}(x,t) = \phi_{ij}(x)\theta(t)$, the governing (28a) becomes

$$\frac{\theta'(t)}{\theta(t)} = \frac{\frac{\partial}{\partial x}\left[\kappa_{ij}(x)\frac{\partial \phi_{ij}(x)}{\partial x}\right]}{\phi_{ij}(x)} = -\lambda^2 \tag{29}$$

where λ is the eigenvalue, and $\phi_{ij}(x)$ and $\theta(t)$ are temporal and spatial eigenfunctions, respectively. In general, there are a number of eigenvalues $\lambda_m (m = 1, 2, 3, \ldots)$ to satisfy the boundary conditions. For each eigenvalue, the solution of temporal function is

$$\theta_m(t) = C_m \cdot e^{-\lambda_m^2 t} \tag{30}$$

where C_m is a coefficient. The corresponding spatial distribution equation is given by

$$\frac{\partial}{\partial x}\left[\kappa_{ij}(x)\frac{\partial \phi_{ij}(x)}{\partial x}\right] + \lambda_m^2 \phi_{ij}(x) = 0 \tag{31}$$

Replacing the position-dependent diffusivity with a linear function (26), (31) is simplified into

$$\left(x + \frac{b_{ij}}{k_{ij}}\right)\frac{\partial^2 \phi_{ij}(x)}{\partial x^2} + \frac{\partial \phi_{ij}(x)}{\partial x} + \frac{\lambda_m^2}{k_{ij}}\phi_{ij}(x) = 0 \tag{32}$$

which can be transformed to Bessel equation, and detail derivation is described in Appendix B [46]. The analytical solution of (32) is given by

$$\phi_{ij,m}(x) = A_{ij,m} J_0\big(\omega_{ij,m}(x)\big) + B_{ij,m} Y_0\big(\omega_{ij,m}(x)\big) \tag{33}$$

where $A_{ij,m}$ and $B_{ij,m}$ are the coefficients to be determined, $J_0(\omega_{ij,m}(x))$ and $Y_0(\omega_{ij,m}(x))$ are the zero-order Bessel functions of the first and second kinds, respectively, and $\omega_{ij,m}(x)$ is represented by

$$\omega_{ij,m}(x) = \frac{2\lambda_m}{\sqrt{k_{ij}}}\sqrt{x + \frac{b_{ij}}{k_{ij}}}. \tag{34}$$

Based on the temporal function (30) and spatial function (33), the general solution for (28) is an infinity series, which is given by

$$\hat{\sigma}_{ij}(x,t) = \sum_{m=1}^{\infty} \theta_m(t) \cdot \phi_{ij,m}(x). \tag{35}$$

Once the general solution is obtained, we need to determine eigenvalues λ_m and eigenfunctions (33). In general multisegment interconnect trees, branch ij with node i and j is the fundamental element, and connects with each other through the junction nodes. Therefore, boundary information at x_i and x_j is critical to determine the coefficients and eigenvalues in (33). Accordingly, the general solutions (33) and their derivatives at x_i and x_j are, respectively, formulated in (36) and (37), as shown at bottom of the page, where $\gamma_{ij,m}(x)$ is written as

$$\gamma_{ij,m}(x) = \frac{\lambda_m}{\sqrt{k_{ij}}\sqrt{x + \frac{b_{ij}}{k_{ij}}}}. \tag{38}$$

In [46], Bessel functions also have (39), as shown at bottom of tha page. Based on (36), (37), and (39), the inward normal component of atom flux on both ends of branch ij can be calculated by

$$\begin{bmatrix} \left.\frac{\partial \phi_{ij,m}(x)}{\partial x}\right|_{x=x_i} \cdot n_i \\ \left.\frac{\partial \phi_{ij,m}(x)}{\partial x}\right|_{x=x_j} \cdot n_j \end{bmatrix} = \begin{bmatrix} D_{11} & D_{12} \\ D_{21} & D_{22} \end{bmatrix} \cdot \begin{bmatrix} \phi_{ij,m}(x_i) \\ \phi_{ij,m}(x_j) \end{bmatrix} \tag{40}$$

where the elements D_{11}, D_{12}, D_{21}, and D_{22} are described in (41), as shown at the bottom of the page.

To satisfy the conservation of the atom flux at junction nodes and block boundaries, substituting (35) and (40) to the BCs (28c) and (28d), we obtain

$$\mathbf{K}(\lambda_m) \cdot \boldsymbol{\phi} = \mathbf{0} \tag{42}$$

$$\begin{bmatrix} \left.\frac{\partial \phi_{ij,m}(x)}{\partial x}\right|_{x=x_i} \\ -\left.\frac{\partial \phi_{ij,m}(x)}{\partial x}\right|_{x=x_j} \end{bmatrix} = \begin{bmatrix} -\gamma_{ij,m}(x_i)J_1\big(\omega_{ij,m}(x_i)\big) & -\gamma_{ij,m}(x_i)Y_1\big(\omega_{ij,m}(x_i)\big) \\ \gamma_{ij,m}(x_j)J_1\big(\omega_{ij,m}(x_j)\big) & \gamma_{ij,m}(x_j)Y_1\big(\omega_{ij,m}(x_j)\big) \end{bmatrix} \cdot \begin{bmatrix} A_{ij,m} \\ B_{ij,m} \end{bmatrix} \tag{36}$$

$$\begin{bmatrix} \phi_{ij,m}(x_i) \\ \phi_{ij,m}(x_j) \end{bmatrix} = \begin{bmatrix} J_0\big(\omega_{ij,m}(x_i)\big) & Y_0\big(\omega_{ij,m}(x_i)\big) \\ J_0\big(\omega_{ij,m}(x_j)\big) & Y_0\big(\omega_{ij,m}(x_j)\big) \end{bmatrix} \cdot \begin{bmatrix} A_{ij,m} \\ B_{ij,m} \end{bmatrix} \tag{37}$$

$$J_1\big(\omega_{ij,m}(x)\big)Y_0\big(\omega_{ij,m}(x)\big) - J_0\big(\omega_{ij,m}(x)\big)Y_1\big(\omega_{ij,m}(x)\big) = \frac{2}{\pi\,\omega_{ij,m}(x)} \tag{39}$$

$$\begin{aligned} D_{11} &= \gamma_{ij,m}(x_i)\frac{J_0\big(\omega_{ij,m}(x_j)\big)Y_1\big(\omega_{ij,m}(x_i)\big) - J_1\big(\omega_{ij,m}(x_i)\big)Y_0\big(\omega_{ij,m}(x_j)\big)}{J_0\big(\omega_{ij,m}(x_i)\big)Y_0\big(\omega_{ij,m}(x_j)\big) - J_0\big(\omega_{ij,m}(x_j)\big)Y_0\big(\omega_{ij,m}(x_i)\big)} \\ D_{12} &= \gamma_{ij,m}(x_i)\frac{2/\big(\pi\,\omega_{ij,m}(x_i)\big)}{J_0\big(\omega_{ij,m}(x_i)\big)Y_0\big(\omega_{ij,m}(x_j)\big) - J_0\big(\omega_{ij,m}(x_j)\big)Y_0\big(\omega_{ij,m}(x_i)\big)} \\ D_{21} &= \gamma_{ij,m}(x_j)\frac{2/\big(\pi\,\omega_{ij,m}(x_j)\big)}{J_0\big(\omega_{ij,m}(x_i)\big)Y_0\big(\omega_{ij,m}(x_j)\big) - J_0\big(\omega_{ij,m}(x_j)\big)Y_0\big(\omega_{ij,m}(x_i)\big)} \\ D_{22} &= \gamma_{ij,m}(x_j)\frac{J_0\big(\omega_{ij,m}(x_i)\big)Y_1\big(\omega_{ij,m}(x_j)\big) - J_1\big(\omega_{ij,m}(x_j)\big)Y_0\big(\omega_{ij,m}(x_i)\big)}{J_0\big(\omega_{ij,m}(x_i)\big)Y_0\big(\omega_{ij,m}(x_j)\big) - J_0\big(\omega_{ij,m}(x_j)\big)Y_0\big(\omega_{ij,m}(x_i)\big)} \end{aligned} \tag{41}$$

Authorized licensed use limited to: Univ of Calif Riverside. Downloaded on June 24,2026 at 00:44:23 UTC from IEEE Xplore. Restrictions apply.

where $\mathbf{K}$ is an $(p+q)\times(p+q)$ matrix, and the vector is

$$\boldsymbol{\phi}=\left[\phi_{ij,m}(x_1),\phi_{ij,m}(x_2),\ldots,\phi_{ij,m}(x_n)\right]^T. \tag{43}$$

In order to find the solution of the nonlinear transcendental equation $|\mathbf{K}(\lambda_m)|=0$ which is equivalent to (42), Wittrick-Williams (WW) algorithm [45], [47] is proposed to calculate all eigenvalues without missing anyone of them, which is also an extremely efficient method. The method is described as follows. We need to determine the number of eigenvalues between zero and value of μ, which is calculated by

$$N(\mu)=N_{0n}(\mu)+s\left\{\mathbf{K}^{\Delta}(\mu)\right\} \tag{44}$$

where $\mathbf{K}^{\Delta}(\mu)$ is the triangular form of $\mathbf{K}(\mu)$ using Gaussian elimination process, $s\{\cdot\}$ is a sign-count function which returns the number of negative main diagonal elements of the matrix $\mathbf{K}^{\Delta}(\mu)$, and $N_{0n}(\mu)$ is the number of natural eigenvalues on decoupled branches with zero Dirichlet boundary conditions on both ends. Therefore, to decouple branches and find $N_{0n}(\mu)$, the vector $\boldsymbol{\phi}$ is set to $\mathbf{0}$, and (37) on brach ij becomes

$$f_0(\mu)=J_0\big(\omega_{ij,m}(x_i)\big)Y_0\big(\omega_{ij,m}(x_j)\big)-J_0\big(\omega_{ij,m}(x_j)\big)Y_0\big(\omega_{ij,m}(x_i)\big)=0. \tag{45}$$

For positive and large x, Jacobi [46] obtained the approximate Formulas for $J_0(x)$ and $Y_0(x)$, which are, respectively, written as

$$J_0(x)\approx\sqrt{\frac{2}{\pi x}}\cos\Big(x-\frac{\pi}{4}\Big),\ Y_0(x)\approx\sqrt{\frac{2}{\pi x}}\sin\Big(x-\frac{\pi}{4}\Big). \tag{46}$$

Substituting (46) into (45), we have

$$\sin\big(\omega_{ij,m}(x_i)-\omega_{ij,m}(x_j)\big)=0. \tag{47}$$

Therefore, the approximated eigenvalue of (45) is given by

$$\widetilde{\lambda}_m=\frac{m\pi}{\left|\frac{2}{\sqrt{\kappa_{ij}}}\left(\sqrt{x_i+\frac{b_{ij}}{k_{ij}}}-\sqrt{x_j+\frac{b_{ij}}{k_{ij}}}\right)\right|} \tag{48}$$

where $\widetilde{\lambda}_m$ denotes approximate value of λ_m. To correct errors of approximation (46), the accurate number of natural eigenvalues on branch ij is determined by

$$N_{0,ij}(\mu)=\widetilde{N}_{0,ij}(\mu)\pm 1 \tag{49}$$

where $\widetilde{N}_{0,ij}(\mu)$ is the approximated value of $N_{0,ij}(\mu)$, which is written as

$$\widetilde{N}_{0,ij}(\mu)=\left\lfloor\frac{|\omega_{ij,m}(x_i)-\omega_{ij,m}(x_j)|}{\pi}\right\rfloor \tag{50}$$

where $\lfloor x\rfloor$ is the floor function which outputs the greatest integer less than or equal to x. In order to obtain the accurate value of $N_{0,ij}(\mu)$, it is necessary to correct $\widetilde{N}_{0,ij}(\mu)$ with the error ±1, which is the purpose of (49). As shown in Fig. 7, a number of numerical results have shown that all approximate eigenvalues represented by (48) are offset to the left or right with respect to accurate eigenvalues of (45). Fig. 7(a) and (c) shows the approximate eigenvalues are less than the accurate eigenvalues. On the contrary, Fig. 7(b) and (d) shows the opposite. Red number denotes $N_{0,ij}(\mu)$ and green number represents $\widetilde{N}_{0,ij}(\mu)$. Based on the relationship between eigenvalues and $N_{0,ij}(\mu)$ shown in Fig. 7, there are four cases to correct errors of $\widetilde{N}_{0,ij}(\mu)$ and obtain the accurate $N_{0,ij}(\mu)$, which are listed in Table I. The total number of natural eigenvalues is the sum of $N_{0,ij}(\mu)$

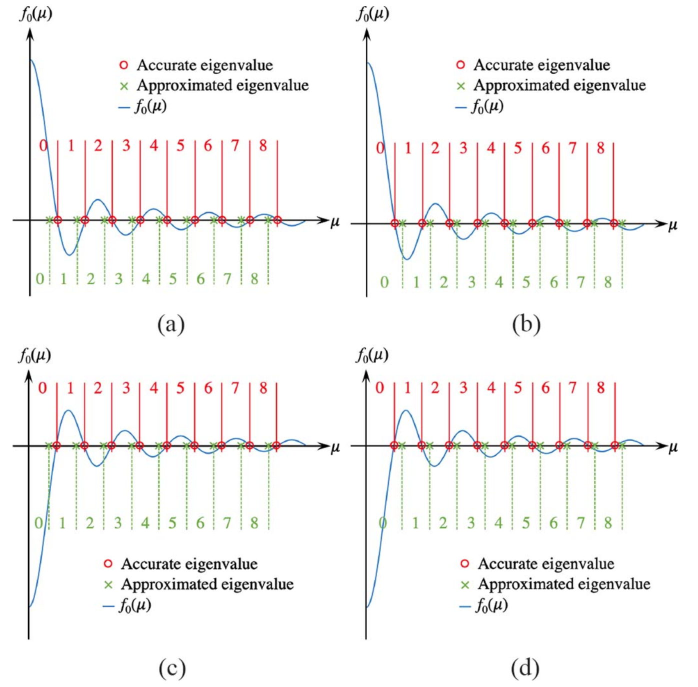

Fig. 7. Four types of relationship between the approximated and accurate eigenvalues to determine $N_{0,ij}(\mu)$ and $\widetilde{N}_{0,ij}(\mu)$. (a) $f_0(0)>0$ and $f_0(\tilde{\lambda}_1)>0$. (b) $f_0(0)>0$ and $f_0(\tilde{\lambda}_1)<0$. (c) $f_0(0)<0$ and $f_0(\tilde{\lambda}_1)<0$. (d) $f_0(0)<0$ and $f_0(\tilde{\lambda}_1)>0$.

$$N_{0n}(\mu)=\sum_{ij}N_{0,ij}(\mu) \tag{51}$$

With the number of eigenvalue (44), we can use bisection method to separate and approach eigenvalues in an iterative way. Once the eigenvalues λ_m are determined, a linear equations formed by BCs (28b)–(28d) are solved for eigenfunctions. For the linear equations, we set some elements such as $A_{12,m}(m=1,2,\ldots)$ to 1 and the coefficients $A_{ij,m}$ and $B_{ij,m}$ can be obtained.

After that, using orthogonality of eigenfunctions and initial conditions (28e), the coefficients C_m can be determined by

$$C_m=\frac{\sum_{ij}\langle\phi_{ij,m}(x)\cdot\hat{\sigma}_{ij}(x,0)\rangle}{\sum_{ij}\langle\phi_{ij,m}(x)\cdot\phi_{ij,m}(x)\rangle} \tag{52}$$

where the inner product is defined by

$$\langle f_{ij}(x)\cdot g_{ij}(x)\rangle=\int_{x_i}^{x_j}f_{ij}(x)g_{ij}(x)\mathrm{d}x. \tag{53}$$

Finally, the original transient hydrostatic stress $\sigma(x,t)$ is obtained by inverse transformation

$$\sigma(x,t)=\sigma(x,\infty)-\hat{\sigma}(x,t). \tag{54}$$

VII. Numerical Results and Discussion

In this section, we present some numerical results and validate the accuracy of the proposed analytical method with

Authorized licensed use limited to: Univ of Calif Riverside. Downloaded on June 24,2026 at 00:44:23 UTC from IEEE Xplore. Restrictions apply.

TABLE I
DETERMINATION OF NUMBER OF NATURAL EIGENVALUES

Figure	Case	Subcase	Correction
Fig. 7(a)	$f_0(0) > 0$ and $f_0(\widetilde{\lambda}_1) > 0$	$\widetilde{N}_{0,ij}(\mu)$ is odd and $f_0(\mu) > 0$	$N_{0,ij}(\mu) = \widetilde{N}_{0,ij}(\mu) - 1$
		$\widetilde{N}_{0,ij}(\mu)$ is even and $f_0(\mu) < 0$	
Fig. 7(c)	$f_0(0) < 0$ and $f_0(\widetilde{\lambda}_1) < 0$	$\widetilde{N}_{0,ij}(\mu)$ is odd and $f_0(\mu) < 0$	
		$\widetilde{N}_{0,ij}(\mu)$ is even and $f_0(\mu) > 0$	
Fig. 7(b)	$f_0(0) > 0$ and $f_0(\widetilde{\lambda}_1) < 0$	$\widetilde{N}_{0,ij}(\mu)$ is odd and $f_0(\mu) > 0$	$N_{0,ij}(\mu) = \widetilde{N}_{0,ij}(\mu) + 1$
		$\widetilde{N}_{0,ij}(\mu)$ is even and $f_0(\mu) < 0$	
Fig. 7(d)	$f_0(0) < 0$ and $f_0(\widetilde{\lambda}_1) > 0$	$\widetilde{N}_{0,ij}(\mu)$ is odd and $f_0(\mu) < 0$	
		$\widetilde{N}_{0,ij}(\mu)$ is even and $f_0(\mu) > 0$	

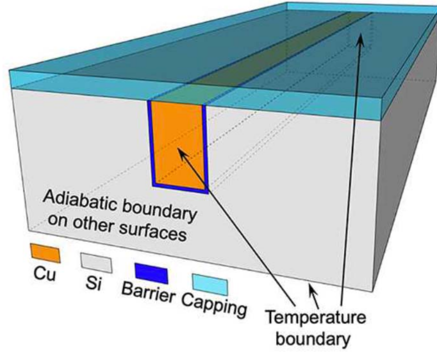

Fig. 8. Single wire structure with thermal boundaries.

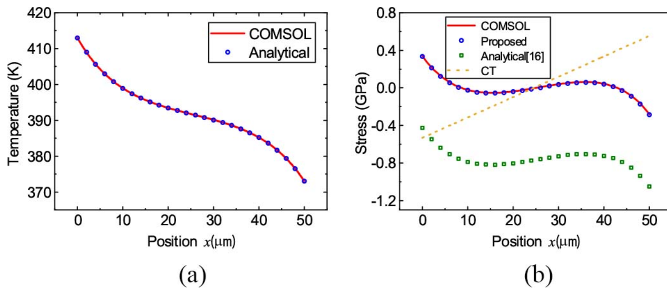

Fig. 9. (a) Temperature distribution. (b) Steady stress distribution of a single wire.

three typical structures in VLSI interconnects, including a single wire, straight line, and multisegment interconnects, as shown in Figs. 8, 11, and 14, respectively. All programs are implemented in MATLAB and tested on a standard computer with a 2.7-GHz i5 CPU, 8-GB memory, and macOS operating system.

A. Single Wire Interconnect Case

Fig. 8 shows the 3-D geometry of a single wire structure with barrier and capping layer. The bottom side is set to a constant temperature T_0, two ends of interconnect are set to

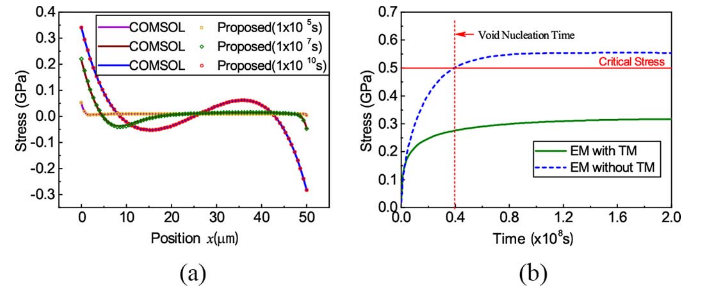

Fig. 10. (a) Transient stress distribution. (b) Maximum stress over time of a single wire.

TABLE II
PARAMETERS FOR THE STRAIGHT LINE INTERCONNECT WIRE

Brch#	j (A/m^2)	L (μm)	Brch#	j (A/m^2)	L (μm)
$l_{1,2}$	−1.06E10	11	$l_{6,7}$	−4.46E10	119
$l_{2,3}$	−5.09E9	119	$l_{7,8}$	−5.76E10	11
$l_{3,4}$	−4.72E10	11	$l_{8,9}$	2.22E10	119
$l_{4,5}$	−4.43E10	119	$l_{9,10}$	1.86E10	11
$l_{5,6}$	−4.41E10	11			

constant temperature T_1 and T_2 and other sides are adiabatic boundary. Current density is 6.6×10^{10} A/m^2, which becomes heat source due to Joule heating. The initial stress σ_0 is set to be 10 MPa. The width of the wire is 0.3 μm and thickness is 0.8 μm. In order to obtain the accurate Γ, COMSOL is employed to perform thermal simulation. Based on (11), the value of Γ is extracted by using the results from COMSOL simulation, which is 9.718×10^{-6} in this case. As shown from Fig. 9(a), the temperature profile computed by the proposed analytical solution (7) agrees very well with the COMSOL simulation.

Once temperature distribution along the single wire is captured, we can obtain the steady-state hydrostatic stress using (23) and (25). Fig. 9(b) shows the proposed method has a good agreement with COMSOL. However, due to using more restricted assumption on boundary conditions, the analytical solution in [16] leads to less accurate results. In Fig. 9(b), the legend "CT" denotes the constant temperature, which represents the case without considering TM effects. As we can see in Fig. 9(b), EM steady-state stress considering TM effects is different from that of "CT" case, and the maximum stress for EM-TM analysis is smaller than that of CT case.

Then, we can perform EM-TM transient analysis. Fig. 10(a) shows that there exists a very good agreement between the proposed method and COMSOL results at different time points. To investigate the impact of TM on transient simulation, the maximum hydrostatic stresses over time of the single wire with and without TM effects are depicted in Fig. 10(b). In this article, we set the critical stress to be 500 MPa [48]. As we can see, If we do not consider TM effects, void will be formed in cathode. In fact, the wire will never fail.

B. Straight Line Interconnect Case

An example of power delivery network (PDN) composed of two metal levels is described in Fig. 11(a). Power and ground lines are illustrated by red and blue lines, respectively. Typical interconnect metals are covered with diffusion barrier (Ta/TaN)

Authorized licensed use limited to: Univ of Calif Riverside. Downloaded on June 24,2026 at 00:44:23 UTC from IEEE Xplore. Restrictions apply.

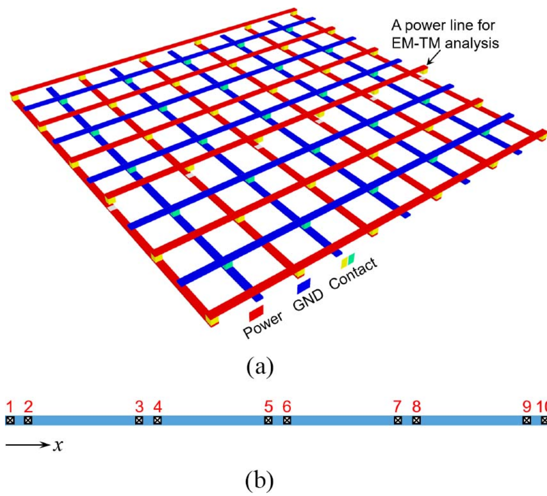

(a)

1 2 3 4 5 6 7 8 9 10

x

(b)

Fig. 11. (a) Structure of a typical PDN. We can evaluate EM stress separately for each power line (red) because diffusion barrier (Ta/TaN) prevents Cu atoms from diffusing into other metal layers. (b) Straight line structure extracted from IBMPG1 benchmark [49], which is drawn from real design. Positive value of current density denotes its direction is along x positive direction.

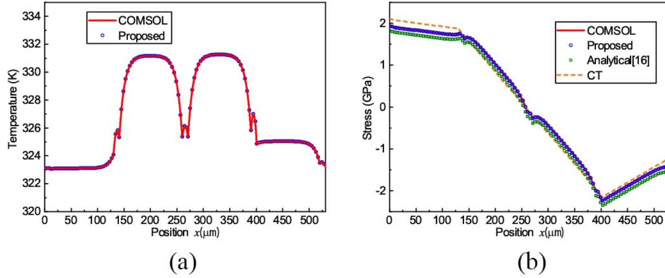

(a) (b)

Fig. 12. (a) Temperature distribution. (b) Steady stress distribution of a straight line.

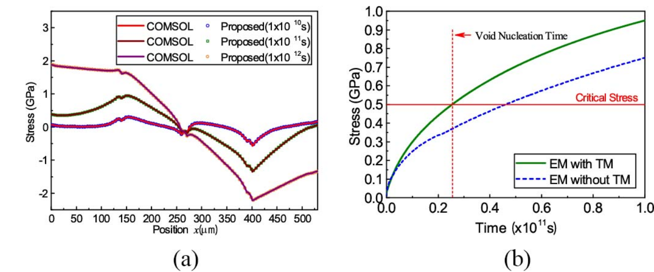

(a) (b)

Fig. 13. (a) Transient stress distribution. (b) Maximum stress over time of a straight line.

layer, which demonstrates strong resistance to EM from one metal layer to another metal layer. Therefore, EM analysis for each continuously connected interconnect can be analyzed separately. For a real application, a straight line is selected from realistic IBMPG1 benchmark [49], as shown in Fig. 11(b). Its size and current densities obtained by SPICE circuits simulation for IBMPG1 benchmark are illustrated in Table II. As we can see, there are global wires (119μm) and local wires (11 μm) in the straight line. For the thermal simulation, Γ calculated by (11) is 9.624×10^{-6}.

Figs. 12 and 13(a) show that there exists a very good agreement between the proposed method and COSMOL results

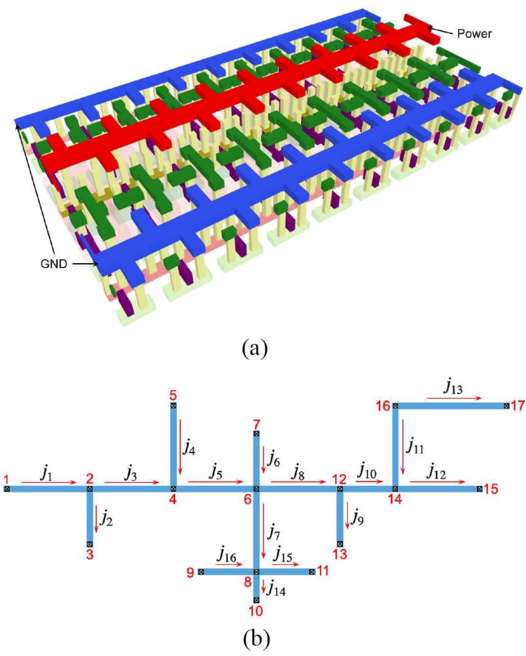

(a)

(b)

Fig. 14. (a) 3-D schematic of standard cell for inverter circuits. Power line (red) is a tree structure in standard cell. We use (b) a multisegment interconnect structure to describe complex power line tree.

TABLE III
PARAMETERS FOR THE MULTISEGMENT INTERCONNECT WIRE

Brch#	j (A/m^2)	L (μm)	Brch#	j (A/m^2)	L (μm)
1	5×10^{10}	30	9	4×10^{10}	20
2	1×10^{10}	20	10	2×10^{10}	20
3	2×10^{10}	30	11	2×10^{10}	30
4	4×10^{10}	30	12	1×10^{10}	30
5	2×10^{10}	30	13	3×10^{10}	40
6	3×10^{10}	20	14	1.5×10^{10}	10
7	2×10^{10}	30	15	1×10^{10}	20
8	5×10^{10}	30	16	2×10^{10}	20

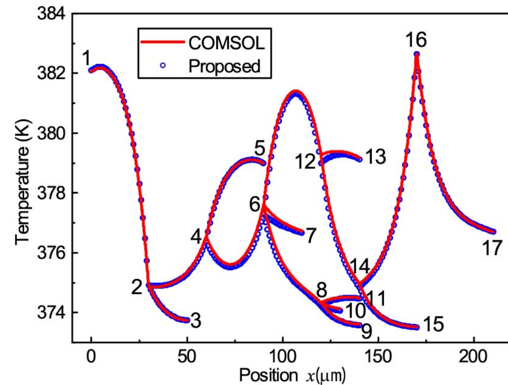

Fig. 15. Temperature distribution of a multisegment interconnect.

for temperature distribution, steady stress and transient stress. It can be observed from Fig. 13(b) that TM effects lead to decreasing of void nucleation time.

C. Multisegment Interconnect Case

To further demonstrate the efficiency and accuracy of the proposed semi-analytical transient solution for EM-TM analysis, we consider power interconnects of standard cell for designing ICs. Fig. 14(a) shows 3-D view of a standard cell

Authorized licensed use limited to: Univ of Calif Riverside. Downloaded on June 24,2026 at 00:44:23 UTC from IEEE Xplore. Restrictions apply.

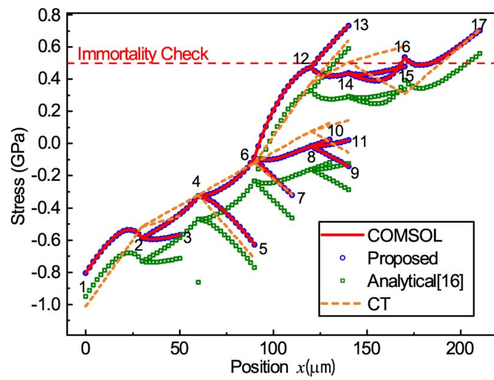

Fig. 16. Steady stress of a multisegment interconnect.

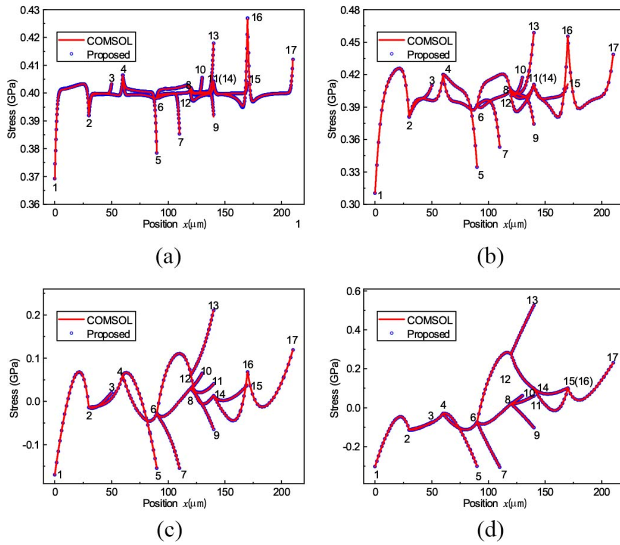

Fig. 17. Transient stress distribution of a multisegment interconnect at (a) $t = 1 \times 10^5$ s, (b) $t = 1 \times 10^6$ s, (c) $t = 1 \times 10^7$ s, and (d) $t = 1 \times 10^8$ s.

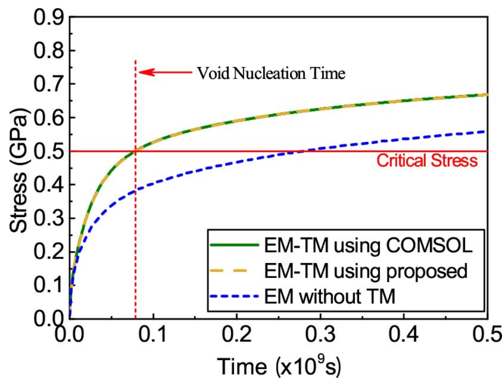

Fig. 18. Maximum stress over time of a multisegment interconnect.

for inverters circuits. As we can see, the power line (red) is a tree structure and has multisegments. Therefore, a more complicated and general multisegment wire structure as shown in Fig. 14(b) is employed as a test case. The current densities and lengths of all the segments are given in Table III, where *Brch* is the branch index, j is the current density, and L is the length of the wire.

We use the proposed analytical method to capture thermal profile due to Joule heating. Accurate Γ and Γ_b are extracted

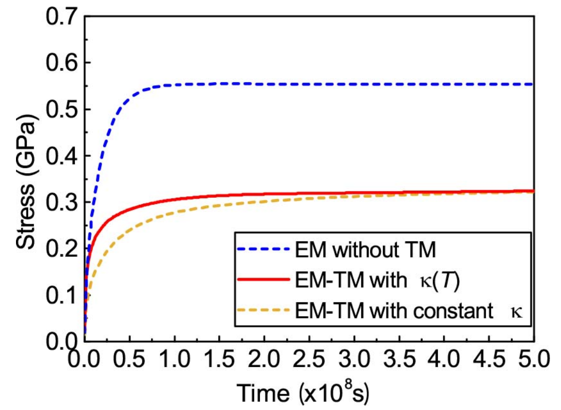

Fig. 19. Maximum stress over time of a single wire for different EM models.

by (11), which are, respectively, 9.615×10^{-6} and 0.0125 for this case. The effective thermal length Γ of the three cases are very similar due to their same dimensions and material in cross view. We set constant temperature at node 2 and 16 with 373 K and 393 K, respectively. Temperature at all nodes is estimated by the thermal solver (20). As we can see that the analytical solution for temperature distribution is very accurate compared to the results of COMSOL as shown in Fig. 15.

Figs. 16 and 17 show that the results from the proposed method have a good agreement with that of COMSOL in both steady and transient analysis. As we can see in Fig. 16, analytical solution of steady state in [16] is again less accurate in the multisegment interconnect case. In addition, the maximum stress of EM-TM analysis is larger than that of CT.

As shown in Fig. 18, the accuracy of our proposed EM-TM method is demonstrated by COMSOL. If we do not consider TM effects, void nucleation time is overestimated. Therefore, based on above mentioned three cases, *TM effects or temperature gradient impacts are significant for accurate prediction of hydrostatic stress evolution*. The TM impacts on EM stress evolution actually depend on the temperature gradient direction and current flow direction of the specific wire segment. The direction of TM driving force is from high temperature to low temperature, and the direction of EM driving force is opposed to that of the current. When the cathode node has lower temperature than the anode node, the TM driving force can attenuate EM driving force as in the single wire case. When the cathode node has higher temperature than the anode node, the TM driving force can enhance EM driving force as shown in the *Brch* 3 of the multisegment interconnect case. Therefore, steady state $\Delta\sigma_{2,4}$ with TM effect is greater than that without TM effect, as shown in Fig. 16. Experiments in [24] and [30] also demonstrated the collective effects of EM and TM. However, the interaction between TM and EM for multisegment interconnect is complex as both two situations exist. Overestimated void nucleation time is the result impacted by the superposition of each branch effect. Another important factor impact void nucleation time is nonuniform diffusivity $\kappa(T)$ [31], which affects time to steady state but does not change the steady results, as shown in Fig. 19. Compared with TM effects, the impact of temperature-dependent diffusivity on void nucleation time is limited.

Authorized licensed use limited to: Univ of Calif Riverside. Downloaded on June 24,2026 at 00:44:23 UTC from IEEE Xplore. Restrictions apply.

TABLE IV
COMPARISON OF PROPOSED METHOD AND COMSOL

	Proposed	COMSOL	Ratio
Time (sec)	31	283	9.1
Memory (MB)	58	617	10.6

Furthermore, to validate the efficiency of the proposed method, time step is set to $\Delta t = 1 \times 10^6$ s and total simulation time lasts 2×10^9 s. Table IV shows that the semi-analytical method reaches a 9.1× or about one order of magnitude speedup over COMSOL (with almost same accuracy) and reduces memory footprint by 10.6× compared with the FEM analysis.

VIII. CONCLUSION

In this article, we have proposed a new semi-analytical transient solution for the EM hydrostatic stress evolution considering TM effects on general multisegment interconnects. The new method is based on the SOV approach to find the analytic solution of coupled EM and TM PDEs. We first develop analytic solutions to compute the steady-state temperature distribution of multisegment wires. Then, we derive a more general and accurate analytical formula for steady state EM-TM stress profile based on the analytical nonuniform temperature profile. Finally, we propose to use piecewise linear technique to approximate the position-dependent diffusivity of metal migration. The numerical results on multisegment interconnects show that the proposed method has negligible error loss compared to COMSOL but is about an order of magnitude faster than COMSOL with 10× less memory footprint. The numerical results further show that temperature gradient due to Joule heating indeed has significant impacts on the EM failure process.

APPENDIX A

There are three types of driving forces leading atomic transport along the interconnect line, such as EM, SM, and TM. EM driving force caused by the momentum transfers between moving electrons and metal atoms increases with the increasing current density due to the applied electrical field. The atomic flux due to EM driving force is defined by

$$J_{\mathrm{EM}} = D_v C_v \frac{eZ\rho j}{k_B T}. \tag{55}$$

A vacancy concentration gradient decreasing from the cathode to the anode because of the migration of metal atoms forms the mechanical stress. The atomic flux caused by the mechanical force is given by

$$J_{\mathrm{SM}} = -D_v \frac{\Omega}{k_B T} C_v \frac{\partial \sigma}{\partial x}. \tag{56}$$

Temperature gradients caused by Joule heating can generate a driving force to the mass flow, namely TM. The atomic flux generated by TM is formulated as

$$J_{\mathrm{TM}} = D_v \frac{Q}{k_B T^2} C_v \frac{\partial T}{\partial x}. \tag{57}$$

The total atomic flux is expressed as [16], [18], [33]–[36]

$$J = -D_v \left(\frac{\Omega}{k_B T} C_v \frac{\partial \sigma}{\partial x} - C_v \frac{eZ\rho j}{k_B T} - \frac{Q}{k_B T^2} C_v \frac{\partial T}{\partial x} \right). \tag{58}$$

The vacancies accumulate or vanish at the divergence of the atomic flux. The vacancy continuity equation can be written as [13], [33]

$$\frac{\partial C_v}{\partial t} = -\frac{\partial J_v}{\partial x} + G \tag{59}$$

where $G = \partial C_L/\partial t$ denotes a generation or annihilation term [50], C_L is the concentration of lattice sites.

Based on Hooke's law, the relationship of lattice concentration and hydrostatic stress is described by

$$\frac{dC_L}{C_L} = -\frac{d\sigma}{B} \tag{60}$$

where B is the Young's modulus. By substituting (60) into (59), we have

$$-\frac{\partial J_v}{\partial x} = \frac{\partial C_v}{\partial t} + \frac{C_L}{B}\frac{\partial \sigma}{\partial t} \tag{61}$$

where the vacancy concentration is represented by [33]

$$C_v = C_{v0} \exp\left(\frac{\Omega \sigma}{k_B T}\right) \tag{62}$$

and its corresponding derivative with respect to time t is

$$\frac{\partial C_v}{\partial t} = C_v \frac{\Omega}{k_B T}\frac{\partial \sigma}{\partial t}. \tag{63}$$

By substituting (63) and (58) into (61), we have

$$\left(\frac{BC_v\Omega}{C_L k_B T} + 1\right)\frac{\partial \sigma}{\partial t} = \frac{\partial}{\partial x}\left[\kappa\left(\frac{\partial \sigma}{\partial x} - \frac{eZ\rho j}{\Omega} - \frac{Q}{\Omega T}\frac{\partial T}{\partial x}\right)\right] \tag{64}$$

where $\kappa = [(BD_vC_v\Omega)/(C_L k_B T)]$ is diffusivity of the stress. Based on the value of EM parameters, Korhonen *et al.* found $[(C_v\Omega)/(k_BT)]/(C_L/B) \ll 1$, which can be neglected, and $C_L = C_v = 1/\Omega$ [40]. Due to the above approximation, (64) can be rewritten as [33]

$$\frac{\partial \sigma}{\partial t} = \frac{\partial}{\partial x}\left[\kappa(x)\left(\frac{\partial \sigma}{\partial x} - \frac{eZ\rho j}{\Omega} - \frac{Q}{\Omega T}\frac{\partial T}{\partial x}\right)\right]. \tag{65}$$

APPENDIX B

As a spatial distribution equation (32) can be transformed into

$$\left(x + \frac{b_{ij}}{k_{ij}}\right)^2 \frac{\partial^2 \phi_{ij}(x)}{\partial x^2} + \left(x + \frac{b_{ij}}{k_{ij}}\right)\frac{\partial \phi_{ij}(x)}{\partial x} + \frac{\lambda_m^2}{k_{ij}}\left(x + \frac{b_{ij}}{k_{ij}}\right)\phi_{ij}(x) = 0. \tag{66}$$

It can be transformed into a general form as

$$u^2 \frac{\partial^2 y}{\partial u^2} + (1-2a)u\frac{\partial y}{\partial u} + \left[b^2c^2u^{2c} + \left(a^2 - c^2p^2\right)\right]y = 0, \quad p \geq 0,\ b > 0 \tag{67}$$

by setting the following transformation relations:

$$\begin{cases} u = x + \frac{b_{ij}}{k_{ij}} \\ a = 0, c = 1/2 \\ b = \frac{2\lambda}{\sqrt{k_{ij}}} \\ p = 0. \end{cases} \tag{68}$$

Authorized licensed use limited to: Univ of Calif Riverside. Downloaded on June 24,2026 at 00:44:23 UTC from IEEE Xplore. Restrictions apply.

Then, replacing $y(u)$ with $u^a z$, (67) can be written as

$$u^2 \frac{\partial^2 z}{\partial u^2} + u \frac{\partial z}{\partial u} + \left(b^2 c^2 u^{2c} - c^2 p^2\right) z = 0. \tag{69}$$

Furthermore, using $t = u^c$, we obtain the Bessel equation

$$t^2 \frac{\partial^2 z}{\partial t^2} + t \frac{\partial z}{\partial t} + \left(b^2 t^2 - p^2\right) z = 0. \tag{70}$$

Therefore, the analytical solution of (67) is given by [46]

$$y(u) = u^a \left[A J_p\left(b u^c\right) + B Y_p\left(b u^c\right)\right] \tag{71}$$

where A and B are the two coefficients, $J_p(\cdot)$ and $Y_p(\cdot)$ are the first and second kind Bessel functions, respectively.

References

[1] S. X.-D. Tan, M. Tahoori, T. Kim, S. Wang, Z. Sun, and S. Kiamehr, *Long-Term Reliability of Nanometer VLSI Systems: Modeling, Analysis and Optimization*. Cham, Switzerland: Springer, 2019.

[2] J. R. Black, "Electromigration—A brief survey and some recent results," *IEEE Trans. Electron Devices*, vol. ED-16, no. 4, pp. 338–347, Apr. 1969.

[3] I. A. Blech, "Electromigration in thin aluminum films on titanium nitride," *J. Appl. Phys.*, vol. 47, no. 4, pp. 1203–1208, 1976.

[4] X. Huang, T. Yu, V. Sukharev, and S. X.-D. Tan, "Physics-based electromigration assessment for power grid networks," in *Proc. IEEE Design Autom. Conf. (DAC)*, Jun. 2014, pp. 1–6.

[5] V. Sukharev, X. Huang, H.-B. Chen, and S. X.-D. Tan, "IR-drop based electromigration assessment: parametric failure chip-scale analysis," in *Proc. IEEE Int. Conf. Comput.-Aided Design (ICCAD)*, Nov. 2014, pp. 428–433.

[6] H.-B. Chen, S. X.-D. Tan, X. Huang, T. Kim, and V. Sukharev, "Analytical modeling and characterization of electromigration effects for multibranch interconnect trees," *IEEE Trans. Comput.-Aided Design Integr. Circuits Syst.*, vol. 35, no. 11, pp. 1811–1824, Nov. 2016.

[7] X. Huang, A. Kteyan, S. X.-D. Tan, and V. Sukharev, "Physics-based electromigration models and full-chip assessment for power grid networks," *IEEE Trans. Comput.-Aided Design Integr. Circuits Syst.*, vol. 35, no. 11, pp. 1848–1861, Nov. 2016.

[8] V. Mishra and S. S. Sapatnekar, "Predicting electromigration mortality under temperature and product lifetime specifications," in *Proc. Design Autom. Conf. (DAC)*, Jun. 2016, pp. 1–6.

[9] Z. Sun, E. Demircan, M. D. Shroff, T. Kim, X. Huang, and S. X.-D. Tan, "Voltage-based electromigration immortality check for general multi-branch interconnects," in *Proc. Int. Conf. Comput.-Aided Design (ICCAD)*, Nov. 2016, pp. 1–7.

[10] X. Huang, V. Sukharev, T. Kim, and S. X.-D. Tan, "Electromigration recovery modeling and analysis under time-dependent current and temperature stressing," in *Proc. IEEE Asia South Pac. Design Autom. Conf. (ASPDAC)*, Jan. 2016, pp. 244–249.

[11] X. Huang, V. Sukharev, and S. X.-D. Tan, "Dynamic electromigration modeling for transient stress evolution and recovery under time-dependent current and temperature stressing," *Integr. VLSI J.*, vol. 55, pp. 307–315, Sep. 2016.

[12] S. Chatterjee, V. Sukharev, and F. N. Najm, "Power grid electromigration checking using physics-based models," *IEEE Trans. Comput.-Aided Design Integr. Circuits Syst.*, vol. 37, no. 7, pp. 1317–1330, Jul. 2018.

[13] S. X.-D. Tan, H. Amrouch, T. Kim, Z. Sun, C. Cook, and J. Henkel, "Recent advances in EM and BTI induced reliability modeling, analysis and optimization," *Integr. VLSI J.*, vol. 60, pp. 132–152, Jan. 2018.

[14] Z. Sun, E. Demircan, M. D. Shroff, C. Cook, and S. X.-D. Tan, "Fast electromigration immortality analysis for multisegment copper interconnect wires," *IEEE Trans. Comput.-Aided Design Integr. Circuits Syst.*, vol. 37, no. 12, pp. 3137–3150, Dec. 2018.

[15] H. Zhao and S. X.-D. Tan, "Postvoiding FEM analysis for electromigration failure characterization," *IEEE Trans. Very Large Scale Integr. (VLSI) Syst.*, vol. 26, no. 11, pp. 2483–2493, Nov. 2018.

[16] A. Abbasinasab and M. Marek-Sadowska, "RAIN: A tool for reliability assessment of interconnect networks—Physics to software," in *Proc. ACM Design Autom. Conf. (DAC)*, New York, NY, USA, 2018, pp. 1–6.

[17] A. Todri, S. Kundu, P. Girard, A. Bosio, L. Dilillo, and A. Virazel, "A study of tapered 3-D TSVs for power and thermal integrity," *IEEE Trans. Very Large Scale Integr. (VLSI) Syst.*, vol. 21, no. 2, pp. 306–319, Feb. 2013.

[18] A. Abbasinasab, *Interconnect Aging—Physics to Software*. Ph.D. dissertation, Elect. Comput. Eng., Univ. California at Santa Barbara, Santa Barbara, CA, USA, Jun. 2018.

[19] X. Wang, Y. Yan, J. He, S. X.-D. Tan, C. Cook, and S. Yang, "Fast physics-based electromigration analysis for multi-branch interconnect trees," in *Proc. IEEE Int. Conf. Comput.-Aided Design (ICCAD)*, Nov. 2017, pp. 169–176.

[20] L. Chen, S. X.-D. Tan, Z. Sun, S. Peng, M. Tang, and J. Mao, "Fast analytic electromigration analysis for general multisegment interconnect wires," *IEEE Trans. Very Large Scale Integr. (VLSI) Syst.*, vol. 28, no. 2, pp. 421–432, Feb. 2020.

[21] K. V. Singh and Y. M. Ram, "Transcendental eigenvalue problem and its applications," *AIAA J.*, vol. 40, no. 7, pp. 1402–1407, 2002.

[22] J. K. Platten, "The Soret effect: A review of recent experimental results," *J. Appl. Mech.*, vol. 73, pp. 5–15, Apr. 2005.

[23] R. Oriani, "Thermomigration in solid metals," *J. Phys. Chem. Solids*, vol. 30, no. 2, pp. 339–351, 1969.

[24] G. Weiling, L. Zhiguo, Z. Tianyi, C. Yaohai, C. Changhua, and S. Guangdi, "The electromigration and reliability of VLSI metallization under temperature gradient conditions," in *Proc. 5th Int. Conf. Solid-State Integr. Circuit Techn.*, Oct. 1998, pp. 226–229.

[25] H. V. Nguyen *et al.*, "Effect of thermal gradients on the electromigration life-time in power electronics," in *Proc. IEEE Int. Rel. Phys. Symp.*, Apr. 2004, pp. 619–620.

[26] K. N. Tu and A. M. Gusak, "A unified model of mean-time-to-failure for electromigration, thermomigration, and stress-migration based on entropy production," *J. Appl. Phys.*, vol. 126, no. 7, 2019, Art. no. 075109.

[27] M. Li, D. W. Kim, S. Gu, D. Y. Parkinson, H. Barnard, and K. N. Tu, "Joule heating induced thermomigration failure in un-powered microbumps due to thermal crosstalk in 2.5D IC technology," *J. Appl. Phys.*, vol. 120, no. 7, 2016, Art. no. 075105.

[28] B. Li, A. Kim, C. Christiansen, R. Dufresne, C. Burke, and D. Brochu, "Thermal characterization and challenges of advanced interconnects (invited)," in *Proc. IEEE Int. Rel. Phys. Symp. (IRPS)*, Apr. 2016, pp. 1–7.

[29] M. Igeta, K. Banerjee, G. Wu, C. Hu, and A. Majumdar, "Thermal characteristics of submicron vias studied by scanning joule expansion microscopy," *IEEE Electron Device Lett.*, vol. 21, no. 5, pp. 224–226, May 2000.

[30] M. F. Abdulhamid, C. Basaran, and Y. Lai, "Thermomigration versus electromigration in microelectronics solder joints," *IEEE Trans. Adv. Packag.*, vol. 32, no. 3, pp. 627–635, Aug. 2009.

[31] Z. Lu, W. Huang, M. R. Stan, K. Skadron, and J. Lach, "Interconnect lifetime prediction for reliability-aware systems," *IEEE Trans. Very Large Scale Integr. (VLSI) Syst.*, vol. 15, no. 2, pp. 159–172, Feb. 2007.

[32] H.-B. Chen, S. X.-D. Tan, J. Peng, T. Kim, and J. Chen, "Analytical modeling of electromigration failure for VLSI interconnect tree considering temperature and segment length effects," *IEEE Trans. Device Mater. Rel.*, vol. 17, no. 4, pp. 653–666, Dec. 2017.

[33] R. De Orio, H. Ceric, and S. Selberherr, "Physically based models of electromigration: From black's equation to modern TCAD models," *Microelectron. Rel.*, vol. 50, no. 6, pp. 775–789, 2010.

[34] X. Zha, "Numerical analysis of lead-free solder joints: Effects of thermal cycling and electromigration," Ph.D. dissertation, Mech. Elect. Manuf. Eng., Loughborough Univ., Loughborough, U.K., Mar. 2016.

[35] J. Xu, "Electromigration simulation of interconnection in very large scare integration," Ph.D. dissertation, Mech. Elect. Manuf. Eng., Binghamton Univ., Binghamton, NY, USA, May 2016.

[36] A. Abbasinasab and M. Marek-Sadowska, "Non-uniform temperature distribution in interconnects and its impact on electromigration," in *Proc. Great Lakes Symp. VLSI (GLSVLSI)*, New York, NY, USA, 2019, pp. 117–122.

[37] C. Cook, Z. Sun, E. Demircan, M. D. Shroff, and S. X.-D. Tan, "Fast electromigration stress evolution analysis for interconnect trees using Krylov subspace method," *IEEE Trans. Very Large Scale Integr. (VLSI) Syst.*, vol. 26, no. 5, pp. 969–980, May 2018.

[38] V. Sukharev and F. N. Najm, "Electromigration check: Where the design and reliability methodologies meet," *IEEE Trans. Device Mater. Rel.*, vol. 18, no. 4, pp. 498–507, Dec. 2018.

[39] H. Zhao and S. X.-D. Tan, "Multi-physics-based FEM analysis for post-voiding analysis of electromigration failure effects," in *Proc. IEEE Int. Conf. Comput.-Aided Design (ICCAD)*, Nov. 2018, pp. 1–8.

[40] M. A. Korhonen, P. Bo/rgesen, K. N. Tu, and C.-Y. Li, "Stress evolution due to electromigration in confined metal lines," *J. Appl. Phys.*, vol. 73, no. 8, pp. 3790–3799, 1993.

Authorized licensed use limited to: Univ of Calif Riverside. Downloaded on June 24,2026 at 00:44:23 UTC from IEEE Xplore. Restrictions apply.

[41] X. Wang, H. Wang, J. He, S. X.-D. Tan, Y. Cai, and S. Yang, "Physics-based electromigration modeling and assessment for multi-segment interconnects in power grid networks," in *Proc. Design Autom. Test Europe Conf. (DATE)*, Mar. 2017, pp. 1727–1732.

[42] Y.-K. Cheng, C.-H. Tsai, C.-C. Teng, and S.-M. Kang, *Electrothermal Analysis of VLSI Systems*. New York, NY, USA: Kluwer, 2000.

[43] T. Y. Chiang, K. Banerjee, K. Banerjee, and K. C. Saraswat, "Compact modeling and SPICE-based simulation for electrothermal analysis of multilevel ULSI interconnects," in *Proc. IEEE/ACM Int. Conf. Comput.-Aided Design (ICCAD)*, Piscataway, NJ, USA, 2001, pp. 165–172.

[44] M. Pedram and S. Nazarian, "Thermal modeling, analysis, and management in VLSI circuits: Principles and methods," *Proc. IEEE*, vol. 94, no. 8, pp. 1487–1501, Aug. 2006.

[45] R. M. Cotta, *Integral Transforms in Computational Heat and Fluid Flow*. Boca Raton, FL, USA: CRC Press, 1993.

[46] G. N. Watson, *A Treatise on the Theory of Bessel Functions*. Cambridge, U.K.: Cambridge Univ. Press, 1944.

[47] W. H. Wittrick and F. W. Williams, "A general algorithm for computing natural frequencies of elastic structures," *Quart. J. Mech. Appl. Math.*, vol. 24, pp. 263–284, Aug. 1971.

[48] R. Gleixner and W. Nix, "A physically based model of electromigration and stress-induced void formation in microelectronic interconnects," *J. Appl. Phys.*, vol. 86, no. 4, pp. 1932–1944, 1999.

[49] S. R. Nassif, "Power grid analysis benchmarks," in *Proc. Asia South Pac. Design Autom. Conf. (ASPDAC)*, Mar. 2008, pp. 376–381.

[50] J. Clement and C. V. Thompson, "Modeling electromigration-induced stress evolution in confined metal lines," *J. Appl. Phys.*, vol. 78, pp. 900–904, Jun. 1998.

Liang Chen (Student Member, IEEE) was born in 1992. He received the B.E. degree in electromagnetic field and wireless technology from Northwestern Polytechnical University, Xi'an, China, in 2015. He is currently pursuing the Ph.D. degree in electronic science and technology with Shanghai Jiao Tong University, Shanghai, China.

He is currently a Visiting Student with the VLSI System and Computation Laboratory, Department of Electrical and Computer Engineering, University of California at Riverside, Riverside, CA, USA. His current research interests include signal integrity of high-speed interconnects, electrothermal co-simulation of 3-D integrated packages, and electromigration reliability.

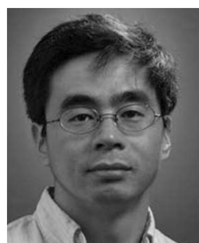

Sheldon X.-D. Tan (Senior Member, IEEE) received the B.S. and M.S. degrees in electrical engineering from Fudan University, Shanghai, China, in 1992 and 1995, respectively, and the Ph.D. degree in electrical and computer engineering from the University of Iowa, Iowa City, IA, USA, in 1999.

He is a Professor with the Department of Electrical Engineering, University of California at Riverside, Riverside, CA, USA, where he also is a Cooperative Faculty Member with the Department of Computer Science and Engineering. His recent research interests include machine learning approaches for VLSI reliability modeling, optimization and management at circuit and system levels, learning-based thermal modeling, optimization and dynamic thermal management for many-core processors, parallel computing and quantum and Ising computing based on GPU and multicore systems. He has published more than 300 technical papers and has coauthored 6 books in the above areas.

Prof. Tan received NSF CAREER Award in 2004. He also received three Best Paper Awards from ICSICT'18, ASICON'17, ICCD'07, and DAC'09. He also received the Honorable Mention Best Paper Award from SMACD'18. He was a Visiting Professor of Kyoto University as a JSPS Fellow from December 2017 to January 2018. He is serving as the TPC Chair of ASPDAC 2021. He also served as the TPC Vice Chair of ASPDAC 2020. He is serving or served as the Editor-in Chief-for *Integration* (Elsevier's), the *VLSI Journal*, and an Associate Editor for three journals the IEEE TRANSACTIONS ON VERY LARGE SCALE INTEGRATION (VLSI) SYSTEMS, the *ACM Transaction on Design Automation of Electronic Systems*, and *Microelectronics Reliability* (Elsevier's).

Zeyu Sun (Student Member, IEEE) received the B.S. degree in electronic and computer engineering from the Hong Kong University of Science and Technology, Hong Kong, in 2015. He is currently pursuing the Ph.D. degree with the Department of Electrical and Computer Engineering, University of California at Riverside, Riverside, CA, USA.

His current research interests include electromigration modeling and assessment and reliability-aware performance optimization.

Shaoyi Peng (Student Member, IEEE) received the B.S. degree in microelectronics from Fudan University, Shanghai, China, in 2016. He is currently pursuing the Ph.D. degree with the Department of Electrical and Computer Engineering, University of California at Riverside, Riverside, CA, USA. He is focusing on VLSI reliability effect modeling and simulation.

Min Tang (Member, IEEE) was born in 1980. He received the B.S. degree in electronic engineering from Northwestern Polytechnical University, Xi'an, China, in 2001, the M.S. degree in electrical engineering from Xi'an Jiao Tong University, Xi'an, in 2004, and the Ph.D. degree in electronic engineering from Shanghai Jiao Tong University, Shanghai, China, in 2007.

Since 2007, he has been a Faculty Member with Shanghai Jiao Tong University, where he is currently an Associate Professor with the Department of Electronic Engineering. He was a Postdoctoral Research Fellow with the University of Hong Kong, Hong Kong, from 2010 to 2012. His research interests include signal and power integrity of high-speed circuits, multiscale, and multiphysics modeling of integrated systems.

Junfa Mao (Fellow, IEEE) was born in 1965. He received the B.S. degree in radiation physics from the National University of Defense Technology, Changsha, China, in 1985, the M.S. degree in experimental nuclear physics from the Shanghai Institute of Nuclear Research, Chinese Academy of Sciences, Beijing, China, in 1988, and the Ph.D. degree in electronic engineering from Shanghai Jiao Tong University, Shanghai, China, in 1992.

Since 1992, he has been a Faculty Member with Shanghai Jiao Tong University, where he is currently a Chair Professor and a Vice President. He was a Visiting Scholar with the Chinese University of Hong Kong, Hong Kong, from 1994 to 1995, and a Postdoctoral Researcher with the University of California at Berkeley, Berkeley, CA, USA, from 1995 to 1996. He has authored or coauthored more than 500 papers (including more than 130 IEEE journal papers). His research interests include the interconnect and package problems of integrated circuits and systems, analysis and design of microwave components and circuits.

Authorized licensed use limited to: Univ of Calif Riverside. Downloaded on June 24,2026 at 00:44:23 UTC from IEEE Xplore. Restrictions apply.